Energy Dissipation in Polymer-Bonded Explosives with Various Levels of Constituent Plasticity and Internal Friction

Amirreza Keyhani[a)], Seokpum Kim[b)], Yasuyuki Horie[c)], and Min Zhou[a,1)]

[a)] *The George W. Woodruff School of Mechanical Engineering, School of Materials Science and Engineering, Georgia Institute of Technology, Atlanta, GA 30332-0405, USA*

[b)] *Oak Ridge National Laboratory, P.O. Box 2008, Oak Ridge, TN 37831, USA*

[c)] *(ret.) Air Force Research Lab, Munitions Directorate, 2306 Perimeter Road, Eglin AFB, FL 32542, USA*

Abstract

The ignition of energetic materials (EM) under dynamic loading is mainly controlled by localized temperature spikes known as hotspots. Hotspots occur due to several dissipation mechanisms, including viscoplasticity, viscoelasticity, and internal friction along crack surfaces. To analyze the contributions of these mechanisms, we quantify the ignition probability, energy dissipation, damage evolution, and hotspot characteristics of polymer-bonded explosives (PBXs) with various levels of constituent plasticity of the energetic phase and internal crack face friction. Using PBX9501 consisting of HMX (Octahydro-1,3,5,7-Tetranitro-1,2,3,5-Tetrazocine) and Estane as a reference material, we analyze variants of this material with several values of the yield stress of the energetic phase and coefficients of internal crack face friction, while other parameters are kept unchanged. The impact loading involves piston velocities between 200 and 1,200 m/s. The analysis uses a Lagrangian cohesive finite element framework that explicitly accounts for finite-strain elastic-viscoplastic deformation of the grains, viscoelastic deformation of the binder, arbitrary crack initiation and propagation in the grains and the binder, debonding between the grains and the binder, contact between internal surfaces, friction and frictional heating along internal surfaces, heat generation resulting from inelastic bulk deformation, and heat conduction. To determine the ignition status of the material or "go" or "no-go" state, we use a criterion based on a criticality threshold obtained from chemical kinetics calculations. For PBX with various levels of HMX plasticity and friction, the probability of ignition, the evolution of dissipation caused by plasticity and friction, the density of cracks, and the locations of cracks are quantified. Results show that samples with higher levels of constituent plasticity (lower yield strengths) or lower levels of internal friction are less likely to ignite. The relative importance of plasticity and friction depends on load intensity, with frictional heating decreasing as load intensity increases. Although the overall viscoplastic heating outweighs the overall frictional heating, friction plays a very important role in hotspot development at all load intensities analyzed, owing to the fact that frictional heating is more localized than viscoplastic heating. The predicted thresholds and ignition probabilities are expressed in a load intensity-duration relation for PBX with different constituent properties.

Keywords: PBX, Energetic materials, Energy dissipation, Ignition threshold

[1] To whom correspondence should be addressed, Tel: 404-894-3294, Fax: 404-894-8336, Email: min.zhou@gatech.edu

1. Introduction

The generation and development of hotspots are key factors in the ignition of energetic materials (EM). Even though the overall bulk temperature of EM is too low to ignite, the formation of hotspots causes localized ignition of EM, which determines the materials' sensitivity [1, 2]. Despite general agreement that the formation of hotspots results in ignition and hotspots arise from heating due to rapid large deformation, a controversy about which mechanisms led to the formation of hotspots had arisen long before Field et al. [3, 4] provided photographic evidence that several mechanisms were involved, including bulk inelasticity (viscoplasticity, viscoelasticity), inter-particle contact and friction, void collapse, and local inelasticity at crack tips. The fact that the ignition of EM is fundamentally a stochastic phenomenon has led to statistical analyses [5-9].

Among available approaches, computational simulations can enable a more comprehensive understanding of ignition as it permits explicit account of underlying physics and interplays among the mechanisms as they evolve, in ways that may not be possible experimentally today. To quantify ignition based on material microstructure, hotspot characteristics, and loading, Barua et al. [10-12] developed a computational framework for establishing microstructure-performance relationships for heterogeneous energetic materials using mesoscale simulations accounting for most of the dominant factors, including arbitrary combinations of constituents and random variations in microstructural morphologies, finite strain viscoelastic and elastic-viscoplastic deformations, thermo-mechanical coupling, thermal softening, strain rate sensitivity, crack initiation, arbitrary crack propagation, heat generation resulting from inelastic bulk deformation and inter-particle friction, and thermal conduction. This computational framework, called CODEX (Cohesive Dynamics for Explosives), is based on the cohesive finite element method (CFEM). Using this framework, Kim et al. [13] showed that lower grain-binder interfacial strength in PBX samples results in increased sensitivity to ignition. Further work by Kim et al. [14] expanded the study of ignition sensitivity to pressed HMX samples without a binder phase and incorporated the James number (J) proposed by Gresshoff and Hrousis [15] based on the James criterion [16]. They computationally obtained ignition probability distribution maps for materials with a range of grain size [14].

The CFEM has its advantages for modeling the mechanical response of energetic materials at the microstructure level relative to other computational approaches, such as XFEM and the meshless method [17, 18]. The response of EM is significantly affected by internal weak and strong discontinuities. Even though the recently developed XFEM-dislocation dynamics (DD) method can account for micro-scale plastic deformation [19, 20], the accuracy of such approaches decrease significantly when a single element embodies several discontinuities such as cracks and grain boundaries. In addition, as XFEM requires crack definition at the outset of analysis, results from XFEM depend on prior knowledge of the location of initial cracks. Meshless methods, on the other hand, cannot precisely model boundaries and resulting frictional dissipation between internal surfaces, a disadvantage in the analysis of ignition as fracture and frictional heating associated with internal failure are very important for EM. As a Lagrangian method, the CFEM is less suitable for the explicit resolution of voids via meshing when compared with Eulerian methods [21-27].

Although several experimental studies [3, 4, 28-32] have focused on mechanisms responsible for the ignition of EM and further computational studies [10-14, 33, 34] have enhanced understanding of ignition, the contributions of different heating mechanisms and their evolution are not well-understood. For example, while it is known that viscoplasticity [28, 29], viscoelasticity, and internal

fracture and friction [31, 32] all play important roles, there is still significant uncertainty as to which mechanisms dominate in different stages of deformation. At a given load intensity, how do the effects of plasticity and friction evolve? As load intensity increases or as loading transitions from non-shock to shock, does the influence of friction or plasticity increase or decrease? Such questions are hitherto unanswered and motivate this study.

The contributions of dissipation mechanisms to the ignition of EM are heavily affected by material heterogeneity, constituent properties, bonding between constituents, defects, and loading (e.g., impact velocity). In the present study, we perform a systematic computational study that quantifies the contributions of some of the dominant dissipation mechanisms, including fracture, friction, and plastic deformation in a polymer-bounded explosive (PBX) system. The analysis focuses on heat generation in microstructures, damage evolution, and hotspot characteristics. In particular, the size, temperature, location, and rate of development of hotspots are of interest. The framework developed by Barua et al. [11, 12, 33] is used, so factors considered include finite-strain elastic-viscoplastic deformation of grains, viscoelastic deformation of the binder, arbitrary crack initiation and propagation in grains and the binder, debonding between grains and the binder, contact between internal surfaces, friction and frictional heating along internal surfaces, heat generation from inelastic bulk deformation, and the conduction of heat.

The materials are made up of HMX (Octahydro-1,3,5,7-tetranitro-1,3,5,7-tetrazocine) energetic grains and Estane polymer binder. The parametric study involves systematically varying the yield stress of the HMX phase and the coefficients of friction for HMX grains, the Estane binder, and HMX/Estane interfaces. The impact loading is effected by imposing piston velocities between 200 and 1,200 m/s. To determine the ignition status of the material or the "go" or "no-go" state, we use a criterion based on a criticality threshold obtained from chemical kinetics calculations [35]. This criterion, which focuses on the hotspot size and the temperature state, determines criticality. For the PBX materials with various levels of HMX plasticity and material friction, we quantify the probability of ignition as a function of the time duration of loading, the evolution of dissipation due to viscoplasticity and friction, the density of cracks, and the locations of cracks. Finally, the computationally predicted ignition sensitivity and threshold are expressed in a load intensity-load duration relation, providing a form for comparison with experimentally measurable quantities. Details of the overall framework and approach can be found in recent publications [11, 12, 33] and therefore are not repeated here.

2. Framework of analysis

2.1. Material and microstructure

Microstructures used consist of HMX energetic grains and Estane binder, mimicking the attributes of PBX9501. Since simulations of PBX microstructures generated using the Voronoi tessellation yield more realistic results than idealized circular shapes of grains [36], we generated a set of twenty statistically similar microstructure instantiations using the Voronoi tessellation method [33, 36] and used this set for all combinations of loading (piston velocity) and constituent properties. Although PBX9501 theoretically is made up of ~95% HMX and ~5% binder by volume, binder volume fractions in real samples of this material are

actually 23%-26% [37, 38]. This is due to the so-called "dirty binder" effect. Basically, very small HMX particles are absorbed in the binder during preparation, leaving the HMX grains with volume fractions on the order of approximately 74-77%. Therefore, we computationally generated microstructures with an HMX grain volume fraction of 70% and a binder volume fraction of 30%. The average grain size of microstructures is $224.7\ \mu m$. Figure 1(a) shows five out of the twenty microstructures in the sample set. The random variations in microstructure morphology among the samples can be clearly seen. Figure 1(b) shows the size distribution of the HMX grains in the microstructure set, the error bars indicate the range of variations among the samples in the set.

In this study, the reference material is PBX9501 with viscoplastic HMX grains with the yield stress value of $\sigma_0 = 260$ MPa. The coefficients of friction for crack faces in the HMX grains, Estane binder, and HMX/Estane interfaces are $\mu = 0.5$. Using these as baseline reference material properties, we analyzed variants of this material with other four levels of yield stress for HMX grains and two levels of coefficient of internal crack face friction. For sample sets with HMX grain yield stress values lower than 195 MPa, more than 25% of the microstructures do not reach criticality in the analysis timeframe of $5.5\ \mu s$ (see Section 2.3). Therefore, we selected $\sigma_0 = 195$ MPa as the minimum value of yield stress analyzed. On the other hand, samples with yield stress values higher than 520 MPa behave similar to samples with hyperelastic HMX grains; therefore, we chose $\sigma_0 = 520$ MPa as the maximum value of yield stress analyzed. With these maximum and minimum values for the yield stress, we analyzed the variants of the reference material PBX9501 $(\sigma_0 = 260$ MPa, $\mu = 0.5)$ [39] using hyperelastic and viscoplastic models for the HMX grains, the latter of which involves yield stress values of 195, 390, and 520 MPa. In addition, for the reference material, we also analyzed another two sample sets with coefficient of friction values of $\mu = 0.25$ and $\mu = 0.75$. We chose the range of 0.25-0.75 for the coefficient of friction based on the work of Green et al. [40] who experimentally estimated the magnitude of the coefficient of friction for an HMX based PBX to be between $0.3 - 0.7$. Other studies also showed that the coefficient of friction levels in the considered range of 0.25-0.75. For example, the coefficient of friction for PBX9501 is between $0.35 - 0.5$, according to Dickson et al. [41]. In total, we analyzed seven material property sets. In the following figures, the results corresponding to those of the viscoplastic model for HMX grains are referred to by the value of the yield stress (σ_0), and the results corresponding to viscoplastic HMX grains with $\sigma_0 = 260$ MPa but different levels of constituent friction are referred by the value of the coefficient of friction (μ).

2.2. Material behavior

The Lagrangian cohesive finite element framework [11] used entails explicit account of microstructure, constitutive behavior, and interfacial response. While it has the advantage of tracking fracture and internal friction, the Lagrangian CFEM framework is not as attractive as Eulerian methods [21-27] for explicit resolution of voids. Here, we recognize those studies on voids and instead focus on fracture and friction along with bulk viscoplasticity (HMX) and viscoelasticity (binder). The effects of voids can be analyzed within our framework using phenomenological approaches. Such work, along with separate work with explicit resolution of voids by us, is ongoing and will be reported in the future.

2.2.1. Estane binder constitutive model

The constitutive response of the Estane binder is modeled via viscoelastic constitutive relations based on the generalized Maxwell model (GMM) [42],

$$\boldsymbol{\sigma}(t) = \int_0^t 2G(\tau - \tau') \frac{\partial \boldsymbol{\varepsilon}^D}{\partial \tau'} d\tau' + \int_0^t K(\tau - \tau') \frac{\partial \boldsymbol{\varepsilon}^H}{\partial \tau'} d\tau'. \tag{2}$$

Here, $\boldsymbol{\sigma}$ is the Cauchy stress, constant K is the bulk modulus, $\boldsymbol{\varepsilon}^D$ and $\boldsymbol{\varepsilon}^H$ are the deviatoric and hydrostatic components of the Eulerian strain tensor, and t and τ are the physical and reduced times, respectively. We use the following Prony series to account for variations of the shear modulus G with the reduced time τ,

$$G(\tau) = G_\infty + \sum_{i=1}^{N_p} G_i e^{-\frac{\tau}{\tau_i^p}} = G_0 \left(g_\infty + \sum_{i=1}^{N_p} g_i e^{-\frac{\tau}{\tau_i^p}} \right), \tag{3}$$

Where $G_0 = G_\infty + \sum_{i=1}^{N_p} G_i$ is the instantaneous shear modulus at reference temperature T_0, G_∞ is the steady-state shear modulus, and $g_i = G_i / G_0$ is the relative modulus of the i-th term. N_p is the number of terms in the Prony series and τ_i^p are the relaxation times. Reference [11] provides the parameters and calibration techniques used for modelling the Estane binder.

2.2.2. Constitutive model for HMX grains

A brief review of constitutive relations for HMX grains is presented below, and more details can be found in Refs. [11] and [43]. The basic kinematic assumption for the elastic-plastic deformation is

$$\mathbf{F} = \mathbf{F}^e \cdot \mathbf{F}^p, \tag{4}$$

where $\mathbf{F}^e$ and $\mathbf{F}^p$ are the elastic and plastic part of the deformation gradient, respectively. The rate of deformation, $\mathbf{D}$, and the spin tensor, $\boldsymbol{\Omega}$, can be decomposed into elastic and plastic parts according to

$$\begin{aligned} \mathbf{D} &= \mathbf{D}^e + \mathbf{D}^p + \mathbf{D}^t, \text{ and} \\ \boldsymbol{\Omega} &= \boldsymbol{\Omega}^e + \boldsymbol{\Omega}^p. \end{aligned} \tag{5}$$

Thermo-elastic coupling is ignored under the assumption of small elastic strains and independence of the elastic moduli on temperature. Consequently, the Jaumann rate of the Kirchhoff stress, $\hat{\boldsymbol{\tau}}$, can be cast in the form of

$$\hat{\boldsymbol{\tau}} = \mathbf{L} : \left(\mathbf{D} - \mathbf{D}^{p} \right), \tag{6}$$

where $\mathbf{L}$ refers to the tensor of elastic moduli

$$\mathbf{L} = \frac{E}{1+\upsilon}\left[\mathbf{I}' + \frac{\upsilon}{1-2\upsilon}\mathbf{I} \otimes \mathbf{I} \right], \tag{7}$$

in which "$\otimes$" denotes the tensor product of two vectors, E and υ denote the Young's modulus and the Poisson's ratio, and $\mathbf{I}$ and $\mathbf{I}'$ refer to second- and fourth-order identity tensors, respectively. For an isotropically hardening, viscoplastic solid

$$\mathbf{D}^{p} = \frac{3\dot{\bar{\varepsilon}}}{2\bar{\sigma}}\boldsymbol{\tau}', \tag{8}$$

where $\dot{\bar{\varepsilon}}$ is the equivalent plastic strain rate and

$$\boldsymbol{\tau}' = \boldsymbol{\tau} - \frac{1}{3}\left(\boldsymbol{\tau} : \mathbf{I} \right)\mathbf{I}, \;\; \bar{\sigma}^{2} = \frac{3}{2}\boldsymbol{\tau}' : \boldsymbol{\tau}'. \tag{9}$$

Here, $\boldsymbol{\tau}'$ and $\bar{\sigma}$ represent the deviatoric portion of the Kirchhoff stress and the Mises equivalent stress, respectively. The equivalent plastic strain rate $\dot{\bar{\varepsilon}}$ is expressed in the form of

$$\left.\begin{aligned}
&\dot{\bar{\varepsilon}} = \frac{\dot{\bar{\varepsilon}}_1 \dot{\bar{\varepsilon}}_2}{\dot{\bar{\varepsilon}}_1 + \dot{\bar{\varepsilon}}_2}, \\
&\dot{\bar{\varepsilon}}_1 = \dot{\bar{\varepsilon}}_0 \left[\frac{\bar{\sigma}}{g\left(\bar{\varepsilon}, T\right)} \right]^{m}, \\
&\dot{\bar{\varepsilon}}_2 = \dot{\bar{\varepsilon}}_m \exp\left[-a\, g\left(\bar{\varepsilon}, T\right) \right], \\
&g\left(\bar{\varepsilon}, T\right) = \sigma_0 \left(1 + \frac{\bar{\varepsilon}}{\varepsilon_0} \right)^{N} \left\{ 1 - \beta \left[\left(\frac{T}{T_0} \right)^{\kappa} - 1 \right] \right\}.
\end{aligned}\right\} \tag{10}$$

In the above relations, $\dot{\bar{\varepsilon}}_0$ and $\dot{\bar{\varepsilon}}_m$ are reference strain rates, a and m are rate sensitivity parameters for strain rates above 5×10^{4} s^{-1} and below 10^{3} s^{-1}, respectively, and $\bar{\varepsilon} = \int_0^t \dot{\bar{\varepsilon}} dt$ denotes the equivalent plastic strain. Function $g(\bar{\varepsilon}, T)$ describes the quasi-static stress-strain behavior at ambient temperature, where σ_0 refers to the quasi-static yield stress, ε_0 and T_0 present the reference strain and the reference temperature, respectively, N denotes the strain hardening exponent, and β and κ are thermal softening parameters. Table 1 provides the values of the parameters for HMX. Reference [43] provides more details about the strain and strain-rate dependence.

The third-order Birch–Murnaghan isothermal equation of state (B-M EOS) is used to describe the volumetric behavior, i.e.,

$$\tau_h = -\frac{3}{2}K_0 J\left(J^{-\frac{7}{3}} - J^{-\frac{5}{3}}\right)\left[1+\frac{3}{4}\left(K_0' - 4\right)\left(J^{-\frac{2}{3}} - 1\right)\right], \tag{11}$$

where $\tau_h = \tau_{ii}/3 = \left(\tau_{11}+\tau_{22}+\tau_{33}\right)/3$ is the hydrostatic part of the Kirchhoff stress ($p = -\tau_h$ is the pressure), K_0 denotes the bulk modulus, and $K_0' = \left(\partial K_0 / \partial P\right)_{P=0}$. $J = \det(\mathbf{F})$ is the Jacobian, where $\mathbf{F}$ is the deformation gradient. According to Landerville et al. [44], $K_0 = 16.71\,GPa$ and $K_0' = 7.79$.

2.2.3. Cohesive-frictional interface constitutive model

The cohesive finite element method (CFEM) explicitly accounts for arbitrary scenarios of fracture in the samples. In this framework, the cohesive elements inserted between triangular bulk elements follow a bilinear traction-separation law illustrated in Fig. 2. Each node of a bulk element is shared by cohesive elements connected to the element, and each edge of a bulk element is connected to an adjacent bulk element edge through a cohesive element. Before the critical separation of δ_0, separations of a cohesive surface pair are completely recoverable, and partial damage occurs beyond this critical point. Complete separation with no further cohesive strength occurs if the separation surpasses δ_c [45]. Table 2 lists the cohesive parameter values for the interface types in the material considered. At each time step, the entire microstructure is scanned to identify potential interpenetration of all possible contact pairs. A penalty force algorithm is used to strongly discourage/prevent interpenetration and maintain proper contact. Reference [11] provides in depth descriptions of the multi-step contact algorithm. To evaluate frictional heating along and, determine the stick-slip states of, the sliding surfaces, the Coulomb friction law is used. Table 3 lists the friction coefficients for the three interface types in the material.

2.2.4. Heat conduction

Dissipation due to inelastic bulk deformation (viscoplastic or viscoelastic work) and friction along internal crack faces is converted to heat, resulting in temperature increases. Heat conduction is considered via

$$\rho c_v \frac{\partial T}{\partial t} = k\nabla^2 T + \eta \dot{W}^{vp} + \dot{W}^{ve} + \dot{W}^{fric}, \tag{12}$$

where k and c_v refer to thermal conductivity and specific heat, and T and t present temperature and time, respectively. The fraction of plastic work turned into heat, η, is equal to 0.9. $\dot{W}^{vp}$, $\dot{W}^{ve}$, and $\dot{W}^{fric}$ denote the rates of plastic work, viscoelastic dissipation,

and frictional dissipation per unit volume, respectively. The frictional heating rate over volume ΔV with the coefficient of friction μ and surface ΔS is

$$\dot{W}^{fric} = \frac{1}{\Delta V}\int_{\Delta S} \mu \sigma_n v_{rel}\, dS, \tag{13}$$

where σ_n and v_{rel} are the normal stress between the surface pair in contact and the relative sliding velocity, respectively.

2.3. Loading configuration

At the onset of loading, the samples possess the uniform temperature of T = 300 K and are not damaged or loaded. Impact loading is effected by applying a specified boundary velocity at the left edge of the microstructures (see Fig. 3(a)), which is linearly increased from zero to the maximums of 200, 400, 600, 800, 1000, and 1200 m/s with a prescribed linear ramp velocity over the initial 10 ns of loading $(0 \le t \le 10 \text{ ns})$, as shown in Fig 3(b). Vertical motions of the top and bottom boundaries of microstructures are constrained, approximating the planner impact loading under the conditions of macroscopically uniaxial strain. The length of all samples is 15 mm and it takes about $5.5\ \mu s$ for the longitudinal wave to propagate over the entire sample.

2.4. Ignition criterion

To determine the initiation of the HMX phase of PBX samples, we used a hotspot size-temperature ignition criterion developed by Barua et al. [33]. Specifically, a hotspot at or above temperature T possesses sufficient energy for thermal runway (the onset of irreversible chemical decomposition) if its diameter $\left(\text{i.e., } d\left(T\right)\right)$ is equal to or greater than a certain value $\left(\text{i.e., } d_c\left(T\right)\right)$,

$$d\left(T\right) \ge d_c\left(T\right). \tag{14}$$

To identify the critical size-temperature condition of hotspots (right-hand side of Eq. (14)), we employed the work of Tarver et al. [35], which is based on chemical kinetics calculations accounting for multi-step reaction mechanisms and the pressure and temperature dependence of reactants and products [35]. According to the work of Barua et al. [33], a specimen is assumed to proceed to ignition if two or more hotspots in a 3 mm square reach 90% of the critical size-temperature threshold calculated by Tarver et al. [35]. Reference [33] provides more details about this initiation criterion.

2.5. Statistical model

The time to criticality of each sample is determined when sufficient critical hotspots according to the ignition criterion described in Section 2.4 emerge in the sample. For statistical analysis of the initiation time for the whole ensemble (the set of microstructure instantiations) at a given loading velocity, we used the work of Barua et al. [33]. Using Terao's model [46], Barua et al. [33] established a physical foundation for the Weibull distribution interpretation of the probability of time to criticality. In the used model

[33], the time to criticality (t_c) is estimated as a cumulative probability distribution and fitted to the Weibull distribution [47] in the form of

$$P(t) = 1 - e^{-\Phi(t)}, \quad \Phi(t) = \begin{cases} 0 & t < t_0 \\ \left(\dfrac{t - t_0}{\tau} \right)^m & t \geq t_0 \end{cases} \tag{15}$$

where t, t_0, and τ are the time to criticality, the minimal time to criticality below which the probability of ignition is zero, and a time-scaling parameter that affects the slope of the distribution curve, respectively. m is a shape parameter and equal to 2 when stress wave propagation does not involve reflection from boundaries of a sample caused by loading conditions [33].

3. Results and discussion

We quantify the ignition probability, the dissipation mechanisms, the damage evolution, and the hotspot characteristics of PBX9501 and its six variants under piston velocities from 200 m/s to 1,200 m/s. We begin by carrying out CFEM calculations to obtain the temperature field of samples subject to loading under the conditions discussed in Section 2.3. Next, we scan the temperature fields to detect critical hotspots according to Section 2.4. Then, we determine the ignition of samples by finding sufficient critical hotspots and calculate energy dissipation resulting from the most dominant physical mechanisms and the damage evolution in the microstructures. Finally, for relative comparison of ignition sensitivity, we fit our results to a load intensity-load duration relation over the entire range of loading space and material properties.

3.1. Axial stress

The profiles of axial stress (compressive) in a microstructure subjected to a piston velocity of 400 m/s at $t = 0.4\,\mu s$ for PBX9501 and all its variants are compared. Figure 4 shows that lower levels of HMX plasticity causes decreases in the average longitudinal stress. In a homogeneous elastic-plastic solid undergoing plane strain loading, the stress-strain curve follows the constrained or P-wave modulus from the unloaded state to the onset of yielding and then follows the instantaneous bulk modulus. For a given material, the instantaneous bulk modulus is always lower than the constrained modulus, indicating that the stress in an elastic material should never be exceeded by that in an elastic-plastic material. However, Fig. 4 shows the opposite trend, as a result of damage (fracture) induced by the loading event. For higher levels of constituent plasticity, the damage induced is relatively small since plastic deformation reduces the stress levels in the microstructures. However, as stress level increases, the microstructures containing HMX with lower levels of constituent plasticity (higher yield stress levels) show significantly more damage than the microstructures with higher levels of HMX constituent plasticity (lower yield stress levels), causing the axial stress to decrease, as shown in Fig. 4.

3.2. Temperature fields and hotspot characteristics

Variations in microstructure morphology and the levels of constituent plasticity and friction provide perturbations to thermo-mechanical processes, causing temperature distributions to differ. Specifically, Fig. 5 depicts the temperature field of a microstructure subjected to loading at 400 m/s for PBX9501 and its six variants at $t = 0.4\,\mu s$. A comparison of Figs. 5(a)-5(e) reveals that in samples with lower levels of constituent plasticity, the temperature distribution is more localized, leading to more hotspots closer to criticality. A higher level of constituent plasticity results in a lower level of fracture (see Section 3.1), leading to less fracture and friction. Therefore, plasticity inhibits localized heating by friction, resulting in relatively more uniform temperature fields. Figures 5(f) and 5(g) show the temperature fields of the same microstructure but with different levels of internal friction. Unlike variations in the level of constituent plasticity, variations in the coefficient of friction affect primarily the peak temperatures. Fracture and subsequent frictional sliding occur primarily near the binder-grain interfaces. As a result, the peak temperatures occur near the grain-binder boundaries (see Fig. 5). For the criticality analysis in Sections 3.5 and 3.6, only the temperature fields in the HMX grains are taken into account since HMX is the energetic phase. The effects of constituent variations on average and peak temperatures are shown in Figs. 6(a) and 6(b), respectively. Variations in constituent friction affect peak temperatures more than the average temperatures. In addition, lower levels of constituent plasticity correspond to higher peak temperatures, as shown in Fig. 6(b). The average temperature is higher in specimens with lower levels of constituent plasticity except in the region in the vicinity of the wave front since widespread plastic heating begins even in the wave front but the frictional heating does not begin until the wave front has passed through the region and caused fracture. Once the stress wave has passed through a region, the heating in specimens with lower levels of constituent plasticity begins to outpace the heating of specimens with higher levels of constituent plasticity.

The changes in temperature fields as a result of variations in constituent properties affect hotspots characteristics, which determine the ignition status of the material or the "go" or "no-go" state. Figures 7(a)-7(c) use the *R*-value (see Ref. [14]) to quantify the overall hotspot conditions in samples under piston velocities of 200 m/s, 400 m/s, and 600 m/s, respectively. The *R*-value is the ratio between the temperature of a hotspot to the temperature of a critical hotspot of the same size. A hotspot with a value of $R = 1$ is said to have reached criticality, and a hotspot of $R = 0$ is still at an initial temperature of 300 K. Here, hotspots with a temperature equal to or above 305 K are considered in the analyses. Figures 7(a) and 7(b) show the *R* values of a microstructure at 200 m/s at $t = 3\ \mu s$ and at 400 m/s at $t = 0.4\ \mu s,$ respectively. At any given *R* value, the number of hotspots is higher when constituent plasticity is lower or constituent friction is higher. Similarly, Fig. 7(c) shows the *R* curves for this microstructure at 600 m/s at $t = 0.2\ \mu s$. Here, the number of hotspots close to criticality $(R \geq 0.8)$ is higher at lower levels of constituent plasticity or higher levels constituent friction, leading to a higher propensity for ignition.

3.3. Energy analysis

Figure 8 shows the total input work (W) at the time of ignition. The error bars indicate the degree of variation among the microstructures in each sample set. Samples with higher levels plasticity (lower yield stress levels) or lower levels of friction (lower coefficients of friction) require higher overall input work to ignite, which means they are less sensitive to ignition. In addition, at higher piston velocities, the difference in critical input work among all cases tends to be lower in general. Specifically, at 200 m/s,

the variation in the input work among all cases is 79.6% while at 1,200 m/s, the variation is 24.3%. These trends reflect the influences of several competing factors. Specifically, the load intensity affects the work input rate, dissipation rates, the speed at which the stress/shock wave propagates, and thermal conduction in different ways due to the non-linear nature of the material behavior and the underlying thermal-mechanical processes. Figures 9(a)-9(f) show the evolution of two major mechanisms of energy dissipation in energetic materials (viscoplasticity and friction) for all sample sets under piston velocities of 200-600 m/s. Frictional dissipation increases when the amount of plastic deformation of energetic grains decreases as the result of higher yield strength levels, reflecting the fact that fracture and consequent interfacial sliding account for a larger portion of the overall deformation as bulk plasticity decreases. In addition, frictional dissipations are negligible at early stages of deformation and then rapidly increase as the amount of cracks grows under loading (see Figs. 9(a), 9(c), and 9(e)). Viscoplastic dissipation, however, increase linearly from the beginning of loading (see Figs. 9(b), 9(d), and 9(f)).

Dissipations from friction, viscoelasticity, and 90% of viscoplasticity $\left(\eta = 0.9 \text{ in Eq. } 11\right)$ turn into heat, contributing to the formation of hotspots. The amount of dissipation in samples at criticality is affected by the level of constituent plasticity and friction, load intensity, microstructure, and time to ignition. Figures 10(a) and 10(b) show the fraction of the input work dissipated by viscoplastic dissipation $\left(W_p/W\right)$, and frictional dissipation $\left(W_f/W\right)$ in all sample sets at the time of ignition, respectively. For hyperelastic HMX grains, W_p/W vanishes since the microstructural constituents do not undergo plastic deformation. Clearly, at any given load intensity, plastic dissipation decreases when the yield stress increases. The rise and fall in the trend of W_p/W versus piston velocity results from the competition between the intensity of loading and the time to ignition. At higher loading velocities, the rate of plastic deformation increases while the total time of deformation decreases since the samples reach criticality faster. The maximum values of W_p/W for $195 \text{ MPa} \le \sigma_0 \le 390 \text{ MPa}$ and $\sigma_0 = 520 \text{ MPa}$ occur under load velocities of 400 m/s and 600 m/s, respectively. For all levels of yield strength, W_p/W converges to approximately 2%, when the piston velocity exceeds 1,000 m/s. As the piston velocity increases from 200 m/s to 1,200 m/s, the fraction of the input work dissipated by friction $\left(W_f/W\right)$ fluctuates between 0.4% and 2% for samples consisting of viscoplastic grains with $195 \text{ MPa} \le \sigma_0 \le 260 \text{ MPa}$ while monotonically decreases for the $\sigma_0 \ge 390 \text{ MPa}$ and hyperelastic cases. The maximum frictional dissipation occurs in samples with hyperelastic HMX grains and for these samples, W_f/W decreases from 9.1% to 0.92% as the load velocity increases from 200 m/s to 1,200 m/s.

For PBX9501, while overall viscoplastic heating at the whole microstructure level is 4.2-10.9 times (depending on the load intensity and the microstructure morphology) frictional heating, the contributions to the development of hotspots (which are responsible for ignition, not the overall average temperature) are different. To see this, we analyze the local heat generations in hotspots. Figure 11 shows the densities of viscoplastic heating and frictional heating (heat per unit volume of hotspots) in all hotspots with $R \ge 0.6$ at t_{50} for 200, 800, and 1200 m/s. The data is for the 20 random microstructure instantiations in the sample set, so both the averages and the ranges of variation among the 20 samples are shown. At 200 m/s, although overall in the samples viscoplastic heating is 5.2 times frictional heating (Fig. 10), frictional heating dominates and accounts for 76.1% of the heating inside the hotspots (Fig. 11(a)). As the load intensity increases, the contribution of friction decreases and the contribution of plasticity increases.

Specifically at 800 m/s, friction and plasticity each accounts for ~50% of the heating in the hotspots (Fig. 11(b)). At 1,200 m/s, the contribution of friction decreases to ~29.5% and the contribution of viscoplasticity increases to ~70.5% (Fig. 11(c)). The trend is generally consistent with that in Fig. 9. The new insight here is that friction plays an important role in the development of hotspots which are responsible for the ignition and detonation of PBX, even up to the piston velocity of 1,200 m/s. As the trend implies, it is possible that, at much higher load intensities, the effect of friction diminishes. However, it is not clear how high the piston velocity would need to be for that. Unfortunately at the present, the Lagrangian computational framework used here is not suitable for analyzing load intensities higher than what we have already analyzed here. If and when the capability is further developed to a point where such analyses can be accurately carried out, we will extend the study in the future. It is also worth noting that fracture and friction cause dissipation to continue and conditions to evolve behind the loading wave front, in contrast to the case when fracture and friction inside the constituents are not considered [48]. Since this is not a focus of this study, details are not included here.

Figures 12(a) and 12(b) show the total amount of heat generated in the samples (H) and the fraction of input work converted to heat at the time of ignition (H/W), respectively. Even though samples with higher levels of constituent plasticity or lower levels of constituent friction are less sensitive to ignition, these samples undergo more heating up to the time of ignition. The dissipation resulting from bulk viscoplasticity spreads more widely in the material (less localized), resulting in a more uniform temperature field. A sample with a more uniform temperature field is less likely to ignite, as it has fewer and cooler hotspots (see Section 3.2). In addition, although the total amount of dissipation is lower at higher velocities, the dissipation is more localized and concentrated in smaller areas of the materials, leading to ignition. Specifically, the increase in the loading velocity from 200 m/s to 1,200 m/s causes the amount of heat generated to decrease from 543.6 J to 114.1 J for PBX9501. The fraction of input work turned into heat at the time of ignition (H/W) is approximately equal for all cases at a given load intensity level. H/W decreases at higher levels of load intensity since the total amount of dissipation at the time of ignition decreases as a result of shorter durations of deformation prior to the onset of ignition. In particular, an increase in the load velocity from 200 m/s to 1,200 m/s causes H/W to decrease approximately from 25.8% to 8.8% for all sample sets. At a given load intensity level, the discrepancy in H/W among all the material variants is 2.2-4.1%.

3.4. Crack density and distribution

This study assumes that samples are initially defect-free (no voids, no cracks) and that cracks result from loading. The analysis accounts for fracture along all possible types of sites including inside the HMX grains, inside the matrix, and the grain-matrix interfaces. Figures 13(a)-13(f) show the crack density, or crack area per unit volume of the material, at approximately median time to ignition (t_{50}) for all sample sets over the range of piston velocity of 200-1,200 m/s. The density of cracks is higher when the level of constituent plasticity is lower (yield stress higher), illustrating the competition between plastic deformation and fracture (see Section 3.1). Since cracks lead to frictional dissipation, the trend for crack density is similar to that for frictional dissipation (W_f/W). The density of cracks in the binder is negligible due to the fact that the volume fraction of the binder is less than that in the grains and the binder is softer. The crack densities at HMX/Estane interfaces (grain boundaries) are higher than those in the HMX grains

at a piston velocity of 200 m/s while fracture sites in the grains outnumber those at the interfaces at piston velocities above 400 m/s. At higher piston velocities, the variations of the crack density at boundaries among cases decrease since most of grain/matrix sites affected by the stress wave are fractured and further energy dissipation by fracture mostly is accommodated by the grains. These trends are qualitatively consistent with experimental results for PBX9501 reported in the literature. For example, under quasi-static conditions, grain fracture is relatively insignificant and debonding of grains from the binder is the dominant fracture mode, except for pre-damaged HMX grains [49]. At high-strain rates $\left(\text{for example, } 2000\ \text{s}^{-1}\right)$, however, PBX9501 fails via predominantly transgranular fracture of the HMX grains [50].

3.5. Probability distribution of the time to criticality

The probability distribution curves for ignition are constructed based on the "go" / "no-go" analysis [33]. To account for the microstructural stochasticity involved in a material's ignition response, the "go" / "no-go" analysis is performed on twenty statistically similar samples for each of combination of constituent plasticity and internal friction level considered. Figures 14(a)-14(c) show probability distributions of the time to criticality t_c for microstructures with the four levels of constituent plasticity of energetic grains at piston velocities of 200 m/s, 400 m/s, and 600 m/s. In these figures, the symbols represent calculated results and the solid lines represent the corresponding fits to the Weibull distribution. The least square regression method is used to calculate the two parameters in the Weibull distribution, t_0 and τ. For a piston velocity of 200 m/s and a HMX yield stress of $\sigma_0 = 195$ MPa, five out of the twenty microstructures in the sample set did not reach criticality within $5.5\ \mu\text{s}$. We fit the Weibull function to the data for samples that ignite within $5.5\ \mu\text{s}$. The value of the parameters for the Weibull distribution function and the median time to ignition (t_{50}) for each simulation set are listed in Table 4.

Results show that lower levels of constituent plasticity (higher yield strength) or higher levels of constituent friction make microstructures less sensitive to ignition (delayed ignition). In general, samples with longer time to criticality are regarded as "less sensitive." These results are in agreement with the findings in Section 3.2, where the hotspot analysis revealed that lower levels of constituent plasticity or higher levels of constituent friction increase the numbers or the risk factors of hotspots. Figure 15 shows the median time to ignition (t_{50}) as a function of loading velocity. The decrease in t_{50} at higher loading velocities indicates higher likelihood for ignition. The differences in the time to criticality among samples in a set and the mean time to criticality (t_{50}) decrease as the piston velocity increases. Furthermore, the difference in t_{50} for cases with different yield stress levels also decreases as the velocity (load intensity) increases. Specifically, the maximum difference in the median time to ignition (t_{50}) for a piston velocity of 200 m/s is 85.8% and decreases to below 7% as the piston velocity reaches 1,200 m/s, as shown in Fig. 15. In addition, the variation in the time to criticality among the microstructures decreases as plasticity decreases. In Eq. (15), τ affects the overall slope (and spread) of the probability distribution curve for ignition. At each loading velocity, as the level of constituent plasticity increases, τ increases, indicating a wider spread of the probability distribution.

3.6. Ignition threshold

For relative comparison of ignition sensitivity, we fit our results to a load intensity-load duration relation of the form

$$P^2\, t_{50} = C, \tag{16}$$

where P is the average longitudinal stress at the loading site, t_{50} is the median time to criticality, and C is a material-dependent fitting constant. A higher value for C indicates lower ignition sensitivity. Figure 16 shows the average longitudinal stress versus the mean time to criticality for all load levels and sample sets. The results for all material variants are then fit to determine the value of C that best represents the data. The values of C for all material variants are listed in Table 5. This approach provides a convenient method for the relative comparison of sensitivity. In Fig. 16, any event lying to the left of a line has an ignition probability lower than 50% and any event falling to the right of the line has an ignition probability of higher than 50%. Therefore, a more sensitive sample set lays farther to the left in the $P - t_{50}$ space. The results are in agreement with the earlier ignition probability analyses indicating that the specimens with higher levels of constituent plasticity or lower levels of friction are less sensitive.

4. Conclusion

The need to understand and quantify the relative importance of the contributions of plasticity and internal friction to dissipation and heating in polymer-bonded explosives (PBXs) motivates this study. To achieve the objective, we use a Lagrangian cohesive finite element framework to analyze the thermo-mechanical response and ignition behavior of PBX9501 and its variants. The analyses focus on material behavior at various levels of constituent friction, HMX grain plasticity, and load intensity. To this effect, hyperelastic and viscoplastic constitutive models are used. Statistically similar microstructure samples are computationally generated and subjected to monotonic loading with piston velocities of 200-1,200 m/s. The ignition probability, the dissipation mechanisms, the damage evolution, and the hotspot characteristics are quantified and analyzed. The results are compared with available experimental results for PBX9501.

The results show that plastic deformation of the energetic grains of the heterogeneous PBXs significantly influence their response and ignition behavior. Despite more overall heat generation, a higher level of constituent plasticity results in a decreased sensitivity to ignition as it reduces peak temperatures and the number or the risk factor of hotspots. This reduction in localized heating results from significant reduction in the density of fracture sites. Fracture and subsequent crack face friction significantly affect heat generation by facilitating and enabling inelastic deformation and, more importantly, localized frictional heating along crack faces. Energy dissipation from plastic deformation spreads more widely in the material and is less localized. In contrast, dissipation and heating due to friction are more localized and play an important role in the development of hotspots, even up to piston velocities of 1,200 m/s.

The time to ignition is analyzed and quantified using the Weibull distribution function, providing explicit expressions for the ignition probability as a function of load intensity and HMX yield strength. The 50% ignition thresholds obtained are analyzed and

presented in a load-intensity-load duration relation $\left(P^2 t_{50} = C\right)$. The analysis reveals that samples with higher levels of constituent plasticity or lower levels of constituent friction are less sensitive. Finally, it is worthwhile to put the analyses reported here in perspective: obviously, plasticity and fracture/internal friction both can play important roles in the ignition of energetic materials, such that neither should be ignored for the conditions analyzed here (piston velocities up to and somewhat higher than 1,200 m/s) and for realistic PBXs. In the idealized limit case of a fully ductile energetic material incapable of fracture (likely does not exist in reality), plasticity would be the sole heating mechanism leading to ignition. On the other hand in the idealized limit case of a fully brittle energetic material (again likely does not exist in reality), fracture and friction would be the heating mechanisms for ignition. Real materials, like what is modeled here, are in between the two limits and have behaviors that reflect the competition and interplay among the heating mechanisms, microstructure, and loading. This study provides insights into dissipation mechanisms leading to ignition that can be used to sensitize or desensitize polymer-bonded explosives.

Finally, we note that the effects of voids have not been included here. We are aware of no reported studies explicitly accounting for both voids and cracks at the microstructure scale. It will be interesting to account for the interactions between voids and cracks in the future.

Acknowledgements

The authors gratefully acknowledge support from the Defense Threat Reduction Agency (DTRA) (Dr. Allen Dalton). Partial support from the Sandia National Labs Academic Alliance (AA) program is also acknowledged. Calculations are carried out on parallel computers at Dynamic Property Research Laboratory (DPRL) at Georgia Tech.

References

[1] F.P. Bowden, A.D. Yoffe, Initiation and growth of explosion in liquids and solids, 1952.

[2] F.P. Bowden, A.D. Yoffe, Fast reactions in solids, Academic Press, 1958.

[3] J. Field, N. Bourne, S. Palmer, S. Walley, J. Sharma, B. Beard, Philosophical Transactions of the Royal Society of London A: Mathematical, Physical and Engineering Sciences, 339 (1992) 269-283.

[4] J.E. Field, G.M. Swallowe, S.N. Heavens, Proceedings of the Royal Society of London. A. Mathematical and Physical Sciences, 382 (1982) 231-244.

[5] J.K. Dienes, J.D. Kershner, in: 11th International Detonation Symposium, 1998.

[6] J.K. Dienes, J. Middleditch, J.D. Kershner, Q. Zuo, A. Starobin, in: Proceedings of the 12th Symposium (International) on Detonation, 2002.

[7] J.K. Dienes, Q.H. Zuo, J.D. Kershner, Journal of the Mechanics and Physics of Solids, 54 (2006) 1237-1275.

[8] A.L. Nichols, C.M. Tarver, in: 12th International Symposium on Detonation, 2002.

[9] Y. Hamate, Y. Horie, Shock Waves, 16 (2006) 125-147.

[10] A. Barua, Y. Horie, M. Zhou, Proceedings of the Royal Society of London A: Mathematical, Physical and Engineering Sciences, 468 (2012) 3725-3744.

[11] A. Barua, M. Zhou, Model. Simul. Mat. Sci. Eng., 19 (2011) 1-24.

[12] A. Barua, M. Zhou, Mat. Sci. Forum, 673 (2011) 21-33.

[13] S. Kim, A. Barua, Y. Horie, M. Zhou, Journal of Applied Physics, 115 (2014) 174902.

[14] S. Kim, C. Miller, Y. Horie, C. Molek, E. Welle, M. Zhou, Journal of Applied Physics, 120 (2016) 115902.

[15] M. Gresshoff, C.A. Hrousis, in: Proceedings of the 14th International Detonation Symposium, Coeur d'Alene, ID, 2010.

[16] H.R. James, Propellants, Explosives, Pyrotechnics, 21 (1996) 8-13.

[17] T. Belytschko, Y. Krongauz, D. Organ, M. Fleming, P. Krysl, Computer Methods in Applied Mechanics and Engineering, 139 (1996) 3-47.

[18] S. Mohammadi, Extended finite element method: for fracture analysis of structures, John Wiley & Sons, 2008.

[19] A. Keyhani, M. Goudarzi, S. Mohammadi, R. Roumina, Computational Materials Science, 104 (2015) 98-107.

[20] A. Keyhani, R. Roumina, S. Mohammadi, Computational Materials Science, 122 (2016) 281-287.

[21] N.K. Rai, H. Udaykumar, Physical Review Fluids, 3 (2018) 033201.

[22] A. Kapahi, H. Udaykumar, Shock Waves, 25 (2015) 177-187.

[23] N.R. Barton, N.W. Winter, J.E. Reaugh, Modelling and Simulation in Materials Science and Engineering, 17 (2009) 035003.

[24] L. Tran, H. Udaykumar, Journal of propulsion and power, 22 (2006) 959-974.

[25] R.A. Austin, N.R. Barton, J.E. Reaugh, L.E. Fried, Journal of Applied Physics, 117 (2015) 185902.

[26] C.D. Yarrington, R.R. Wixom, D.L. Damm, Journal of Applied Physics, 123 (2018) 105901.

[27] N.K. Rai, H.S. Udaykumar, Physical Review Fluids, 3 (2018) 033201.

[28] R.H. Guirguis, AIP Conference Proceedings, 505 (2000) 647-650.

[29] R.E. Winter, J.E. Field, Proceedings of the Royal Society of London. A. Mathematical and Physical Sciences, 343 (1975) 399-413.

[30] G.M. Swallowe, J.E. Field, Proceedings of the Royal Society of London. A. Mathematical and Physical Sciences, 379 (1982) 389-408.

[31] R. Menikoff, Research Highlights 2005, (2005).

[32] C. Skidmore, D. Phillips, B. Asay, D. Idar, P. Howe, D. Bolme, in: AIP Conference Proceedings, AIP, 2000, pp. 659-662.

[33] A. Barua, S. Kim, Y. Horie, M. Zhou, Journal of Applied Physics, 113 (2013) 064906.

[34] S. Kim, Y. Horie, M. Zhou, Metallurgical and Materials Transactions A, 46 (2015) 4578-4586.

[35] C.M. Tarver, S.K. Chidester, A.L. Nichols, J Phys Chem-Us, 100 (1996) 5794-5799.

[36] Y. Wu, F. Huang, Mechanics of Materials, 41 (2009) 27-47.

[37] E.M. Mas, B.E. Clements, A. Ionita, P. Peterson, AIP Conference Proceedings, 845 (2006) 487-490.

[38] J.B. David, C. Paul, Modelling and Simulation in Materials Science and Engineering, 7 (1999) 333.

[39] R. Menikoff, T.D. Sewell, Combustion theory and modelling, 6 (2002) 103-125.

[40] L. Green, A. Weston, J. Van Velkinburg, in, California Univ., Livermore. Lawrence Livermore Lab., 1971.

[41] P. Dickson, G. Parker, L. Smilowitz, J. Zucker, B. Asay, in: AIP Conference Proceedings, AIP, 2006, pp. 1057-1060.

[42] E.M. Mas, B.E. Clements, B. Blumenthal, C.M. Cady, G.T.G. III, C. Liu, AIP Conference Proceedings, 620 (2002) 661-664.

[43] M. Zhou, A. Needleman, R.J. Clifton, Journal of the Mechanics and Physics of Solids, 42 (1994) 423-458.

[44] A.C. Landerville, M.W. Conroy, M.M. Budzevich, Y. Lin, C.T. White, I.I. Oleynik, Applied Physics Letters, 97 (2010) 251908.

[45] J. Zhai, V. Tomar, M. Zhou, Transactions-American society of mechanical engineers Journal of Engineering Materials and Technology, 126 (2004) 179-191.

[46] K. Terao, Irreversible Phenomena: Ignitions, Combustion, and Detonation Waves, Springer, 2007.

[47] W. Weibull, Ingeniors Vetenskaps Akademien, (1939).

[48] J. Gilbert, K. Gonthier, Meso-Scale Computation of Uniaxial Waves in Granular Explosives-Analysis of Deformation Induced Ignition, in: 50th AIAA Aerospace Sciences Meeting including the New Horizons Forum and Aerospace Exposition, American Institute of Aeronautics and Astronautics, 2012.

[49] P. Rae, S. Palmer, H. Goldrein, J. Field, A. Lewis, in: Proceedings of the Royal Society of London A: Mathematical, Physical and Engineering Sciences, The Royal Society, 2002, pp. 2227-2242.

[50] G.T. Gray, W.R. Blumenthal, D.J. Idar, C.M. Cady, AIP Conference Proceedings, 429 (1998) 583-586.

Tables

Table1. Parameters in the viscoplastic constitutive model of HMX.

σ_0 (MPa)	ε_0	N	T_0 (K)	β
260	5.88×10^{-4}	0.0	293	0.0
$\dot{\varepsilon}_0$ (s^{-1})	m	$\dot{\varepsilon}_m$ (s^{-1})	a (1/MPa)	κ
1×10^{-4}	100.0	8.0×10^{12}	22.5	0.0

Table 2. Cohesive parameters.

Interface type	$\delta_0(\mu m)$	$\delta_c(\mu m)$	$S_{max}(MPa)$
Estane-Estane	0.001	10	38.4
HMX-HMX	0.01	5	101
HMX-Estane	0.049	4.62	35

Table I3. Coefficients of friction for PBX9501 and two variants.

	HMX	Estane	HMX-Estane
PBX9501	0.5	0.5	0.5
$\mu = 0.25$	0.25	0.25	0.25
$\mu = 0.75$	0.75	0.75	0.75

Table 4. Parameters for the adjusted time Weibull distributions.

			200 m/s	400 m/s	600 m/s	800 m/s	1000 m/s	1200 m/s
PBX 9501	$\sigma_0 = 260$ MPa $\mu = 0.5$	t_0 (μs)	2.13	0.29	0.12	0.07	0.04	0.03
		t_{50} (μs)	3.6	0.43	0.18	0.09	0.06	0.04
		τ (10^{-6})	1.77	0.17	0.07	0.02	0.02	0.01
Levels of HMX plasticity	$\sigma_0 = 195$ MPa	t_0 (μs)	2.89	0.1	0.11	0.06	0.04	0.03
		t_{50} (μs)	4.98	0.5	0.17	0.09	0.06	0.04
		τ (10^{-6})	2.51	0.47	0.07	0.03	0.02	0.01
	$\sigma_0 = 390$ MPa	t_0 (μs)	1.13	0.28	0.14	0.07	0.04	0.03
		t_{50} (μs)	1.99	0.4	0.18	0.09	0.05	0.04
		τ (10^{-6})	1.03	0.14	0.05	0.02	0.01	0.01
	$\sigma_0 = 520$ MPa	t_0 (μs)	1.16	0.32	0.12	0.07	0.04	0.03
		t_{50} (μs)	1.89	0.39	0.16	0.09	0.05	0.04
		τ (10^{-6})	0.87	0.08	0.05	0.02	0.01	0.01
	Hyperelastic	t_0 (μs)	1.2	0.3	0.11	0.06	0.04	0.03
		t_{50} (μs)	1.65	0.37	0.15	0.08	0.06	0.04
		τ (10^{-6})	0.55	0.08	0.05	0.03	0.01	0.01
Coefficients of friction	0.25	t_0 (μs)	3.5	0.41	0.19	0.08	0.05	0.04
		t_{50} (μs)	4.71	0.64	0.23	0.11	0.07	0.05
		τ (10^{-6})	1.45	0.28	0.06	0.03	0.02	0.01
	0.75	t_0 (μs)	2.13	0.27	0.09	0.07	0.04	0.03
		t_{50} (μs)	3.29	0.44	0.16	0.09	0.05	0.04
		τ (10^{-6})	1.39	0.21	0.08	0.03	0.02	0.01

Table 5. Parameter C in the load intensity-load duration ignition threshold $\left(P^2\ t_{50} = C\right)$ for PBX9501 and its six variants.

		Levels of HMX plasticity				Coefficients of friction	
	PBX9501	$\sigma_0 = 195$ MPa	$\sigma_0 = 390$ MPa	$\sigma_0 = 520$ MPa	Hyperelastic	$\mu = 0.25$	$\mu = 0.75$
C $\left(10^{12}\ \text{Pa}^2.\text{s}\right)$	3.225	3.608	2.759	2.588	2.212	3.748	3.174

Figures

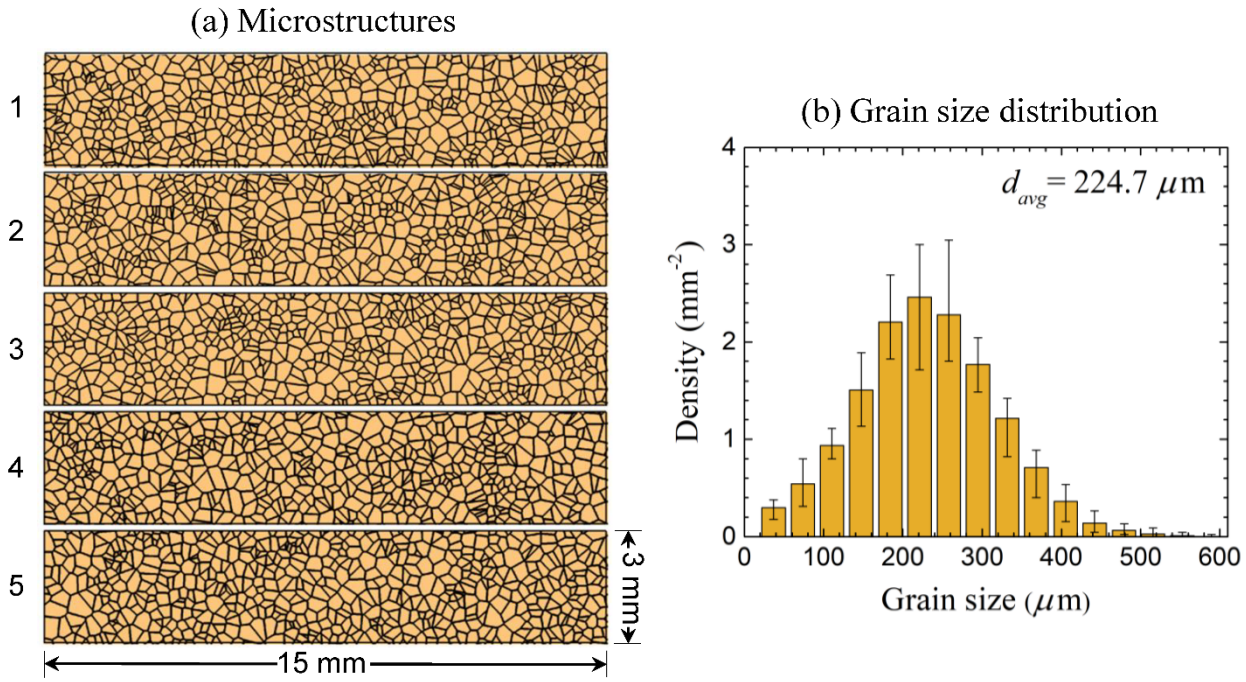

Fig. 1. (a) Five out of twenty computationally generated microstructures with a grain volume fraction of 70%, and (b) size distributions of HMX grains.

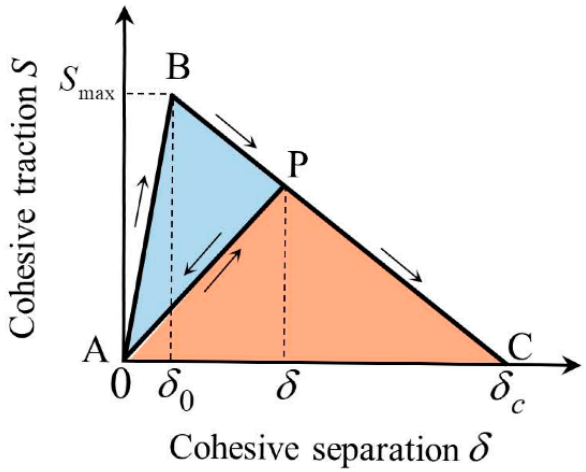

Fig. 2. Bilinear traction-separation law for cohesive elements.

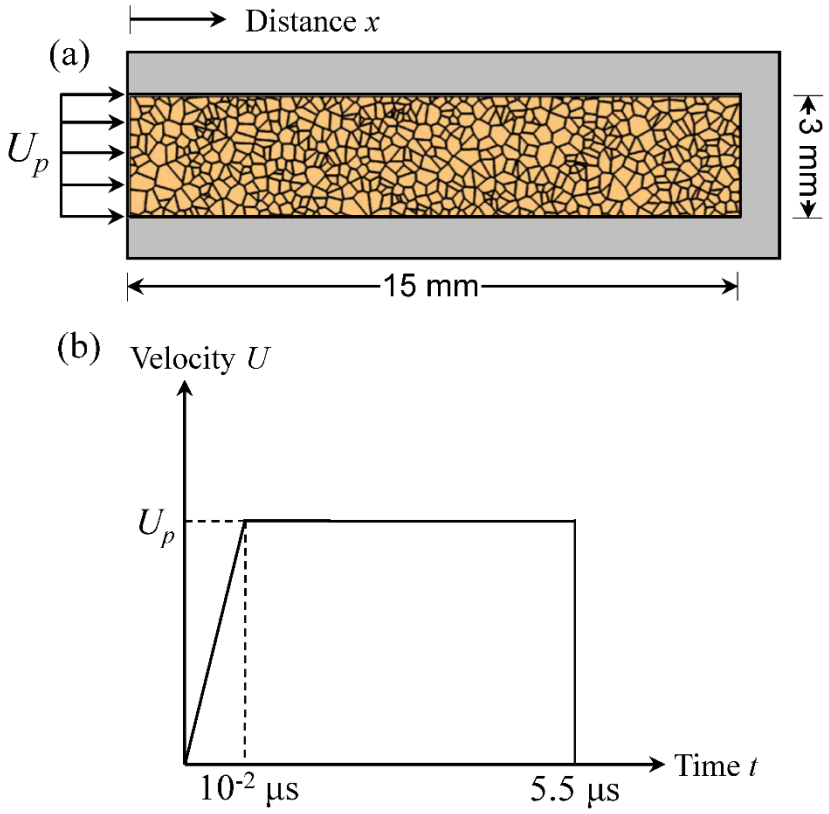

Fig. 3. (a) Loading configuration and boundary conditions considered for simulations, and (b) load history applied on the left edge of the sample.

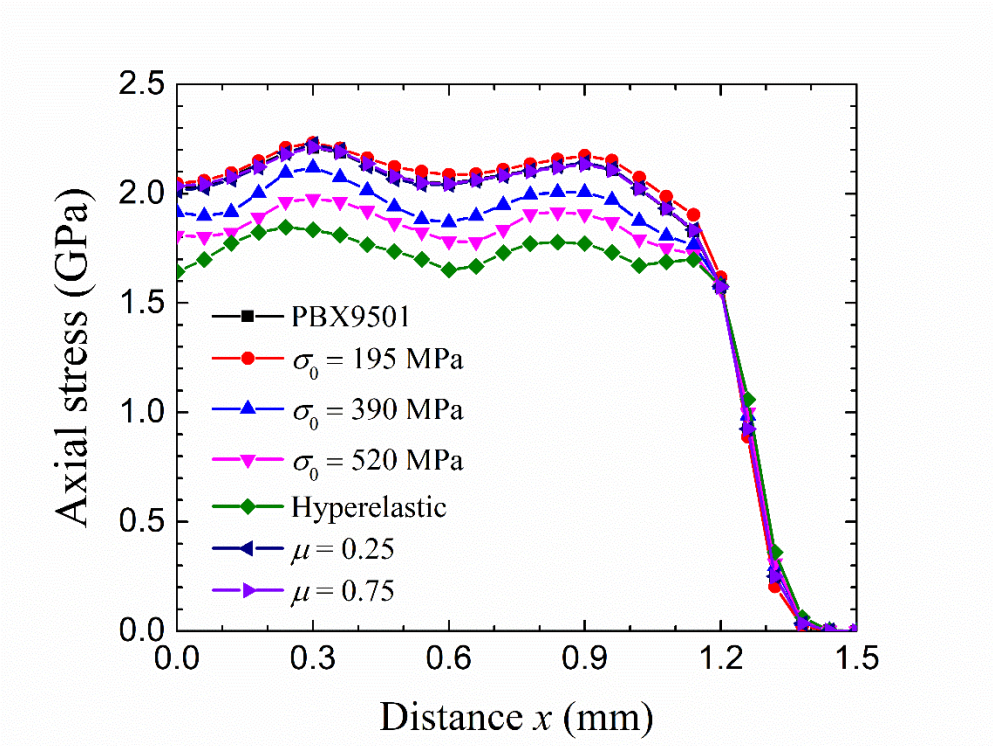

Fig. 4. Profiles of average axial stress at $t = 0.4\,\mu s$ for a microstructure subjected to a piston velocity of 400 m/s.

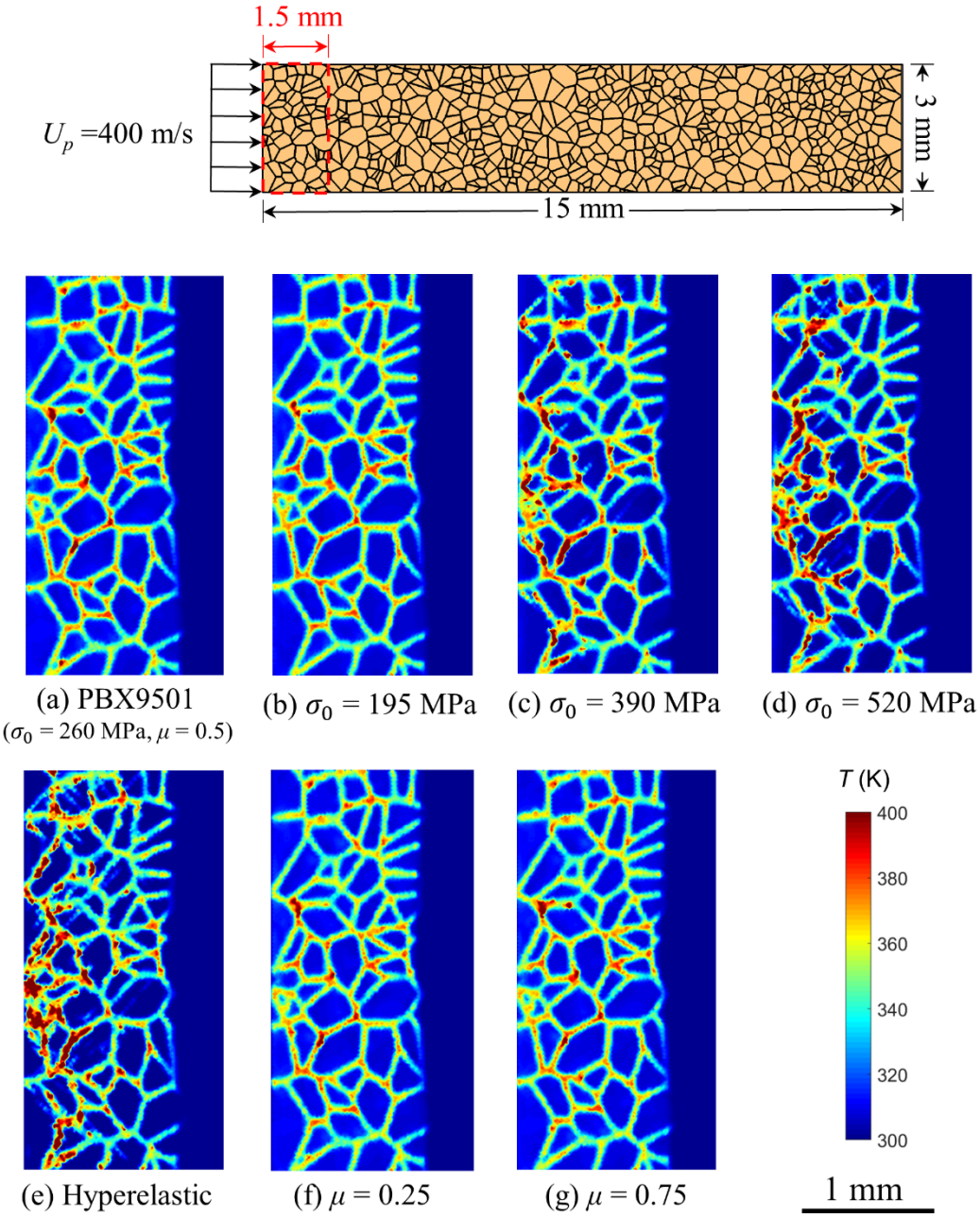

Fig. 5. Temperature fields and hotspot locations for all material cases under a loading velocity of 400 m/s at t = 0.4 μs; (a) PBX9501, (b), (c), and (d) HMX grains with yield stress levels of 195, 390, and 520 MPa, respectively, (e) hyperelastic HMX grains, and (f) and (g) HMX grains with a yield stress level of 260 MPa and coefficients of friction 0.25 and 0.75, respectively. The peak temperatures occur near the boundaries between the binder and the grains.

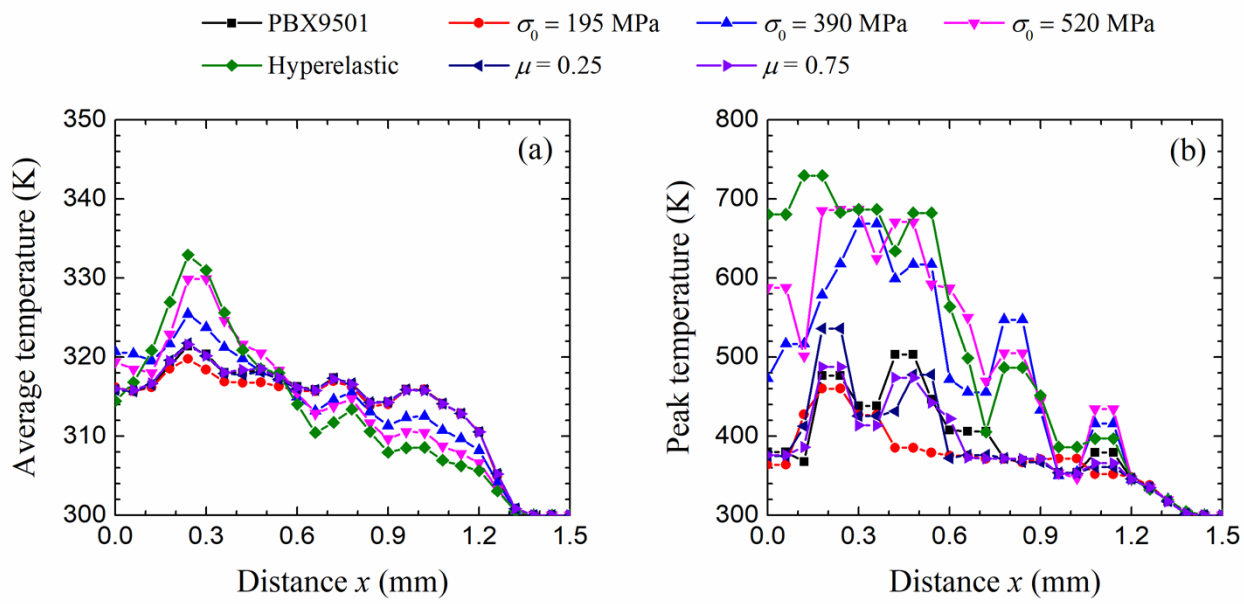

Fig. 6. (a) Profiles of average temperature and (b) profiles of peak temperature corresponding to the same microstructure in Figs. 3 and 4. These figures show the temperature profiles prior to criticality of the samples.

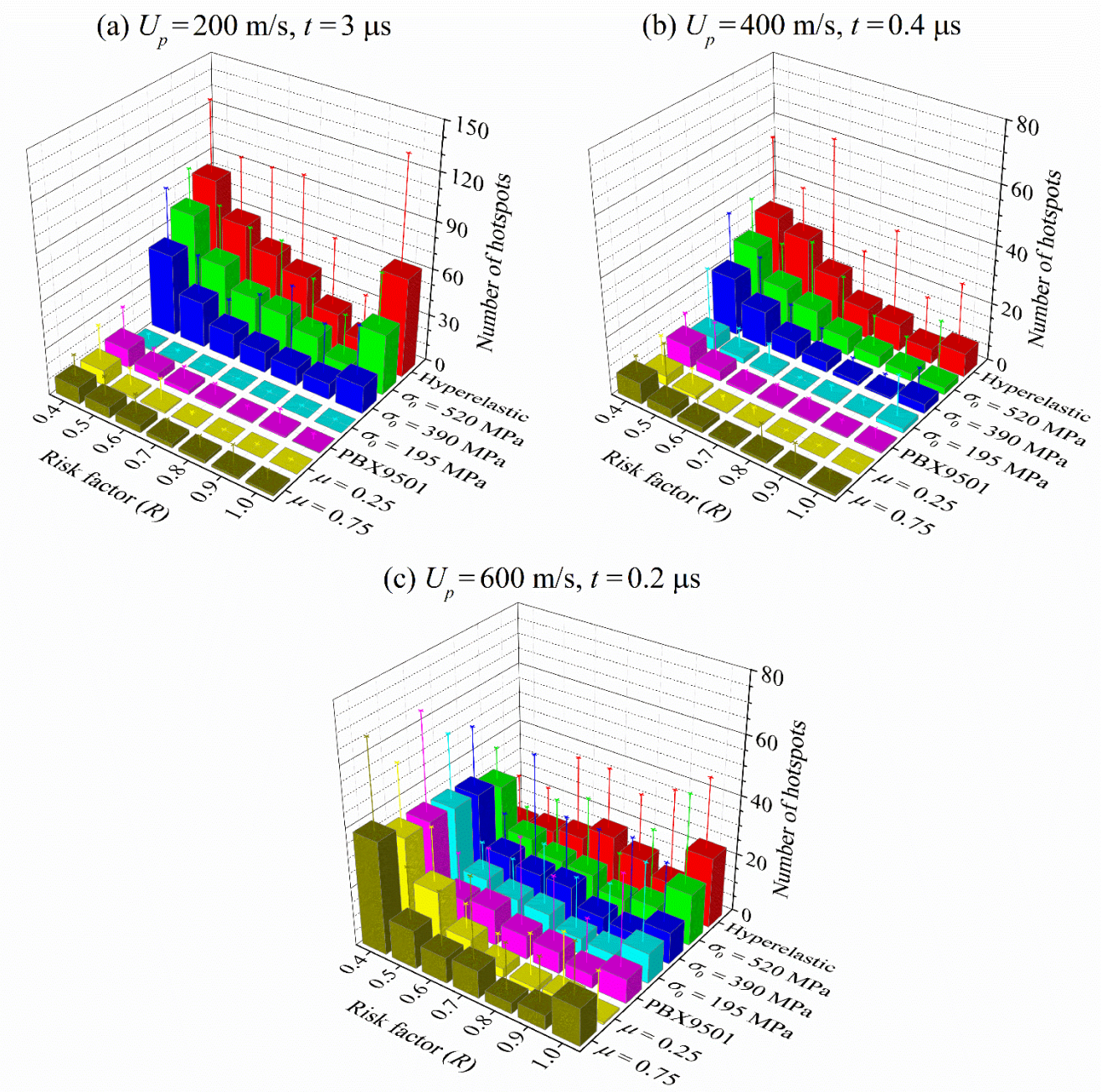

Fig. 7. Comparison of R curves for all material cases; (a) R curves for a microstructure under a loading velocity of 200 m/s at $t = 3$ μs, (b) R curves for a microstructure under a loading velocity of 400 m/s at $t = 0.4$ μs, and (c) R curves for a microstructure under a loading velocity of 600 m/s at $t = 0.2$ μs.

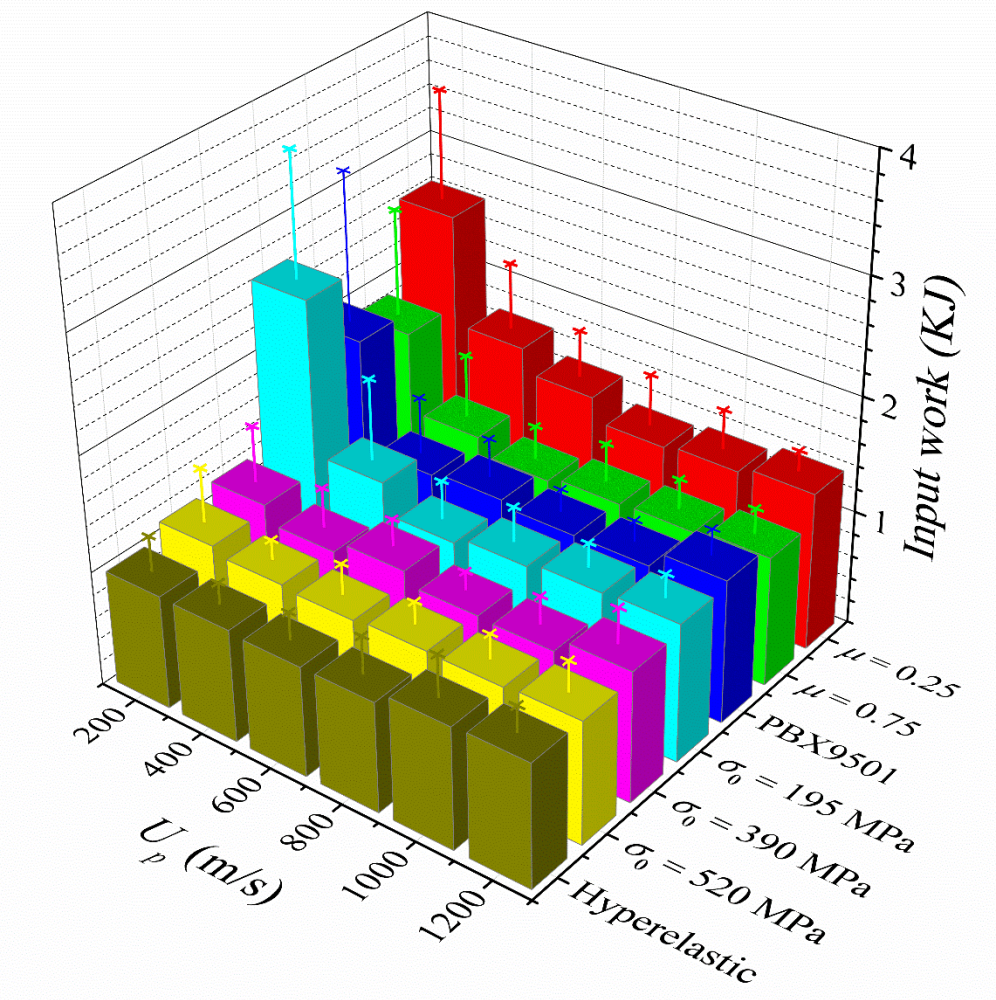

Fig. 8. Comparison of the required input work for ignition for all material cases over the range of piston velocities of 200-1,200 m/s.

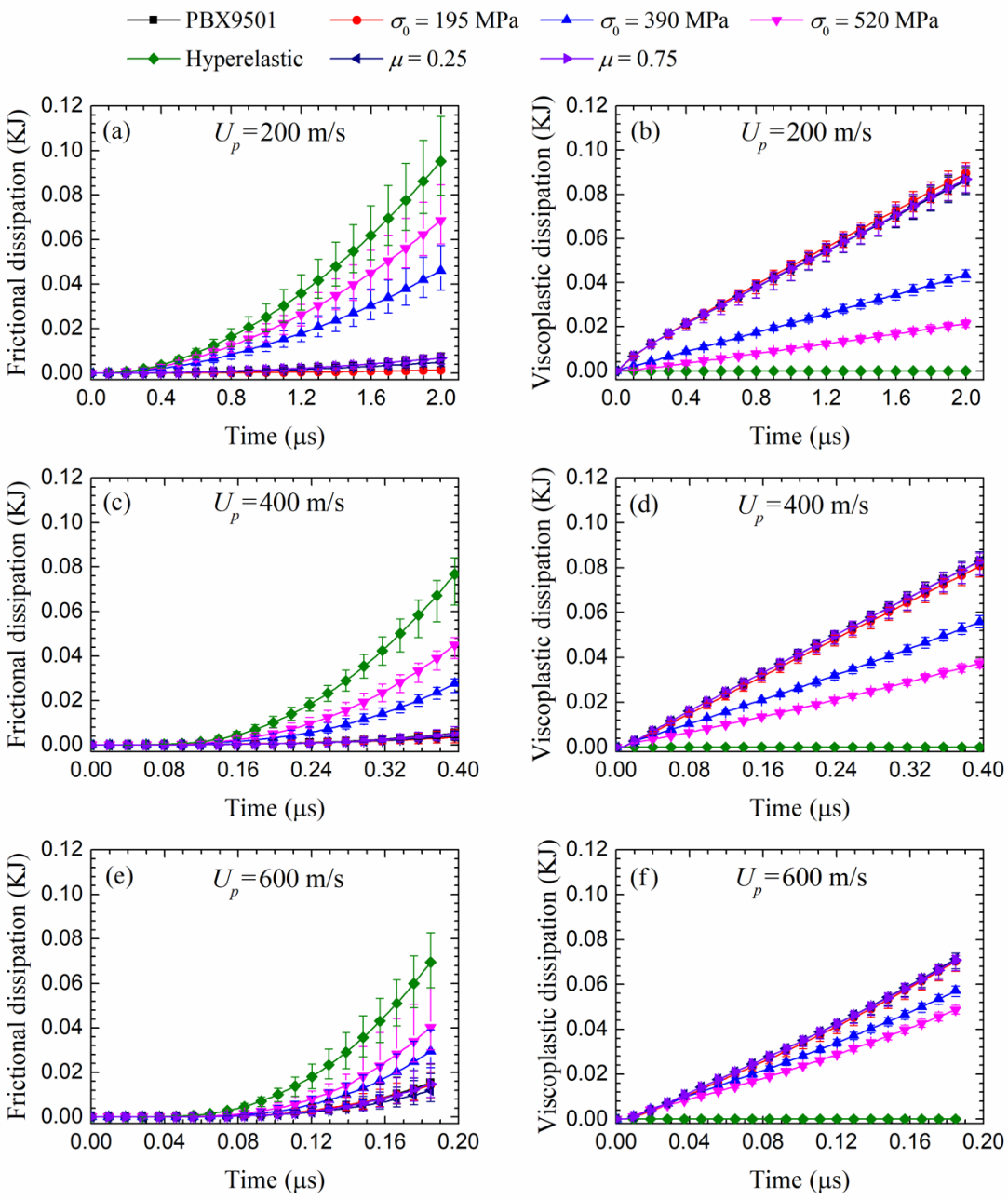

Fig. 9. Evolution of frictional dissipation and viscoplastic dissipation as a function of time for all cases; (a), (c), and (e) frictional dissipation for piston velocities of 200 m/s, 400 m/s, and 600 m/s, respectively, and (b), (d), and (f) viscoplastic dissipation for piston velocities of 200 m/s, 400 m/s, and 600 m/s, respectively.

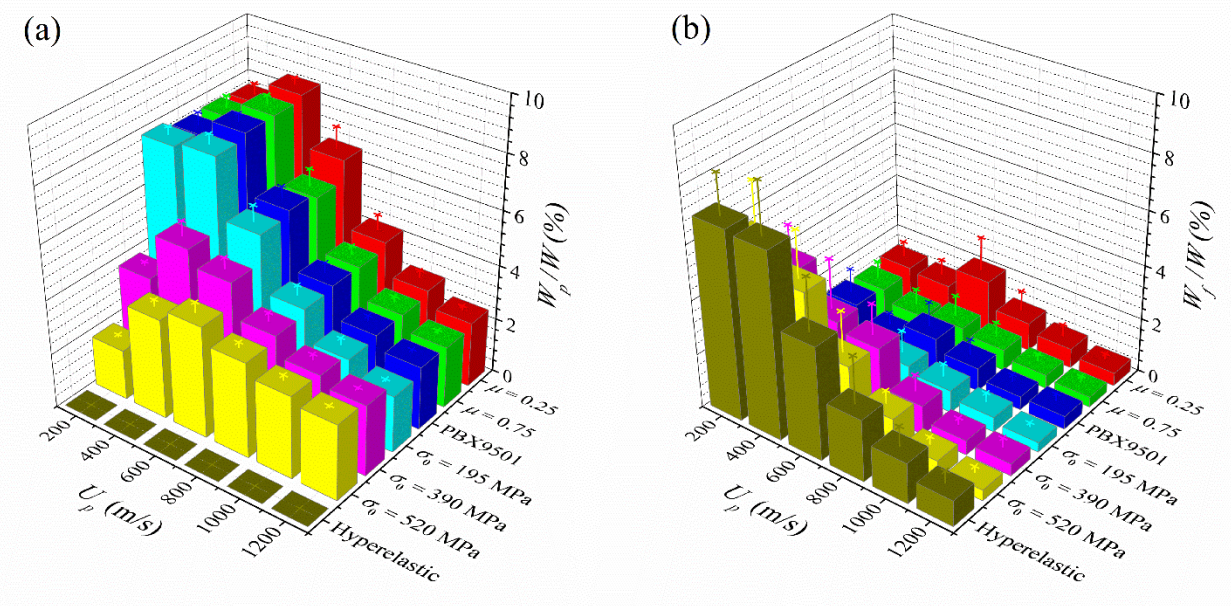

Fig. 10. (a) Fraction of input work dissipated due to plastic deformation of HMX grains, and (b) fraction of input work dissipated due to friction at the time of ignition.

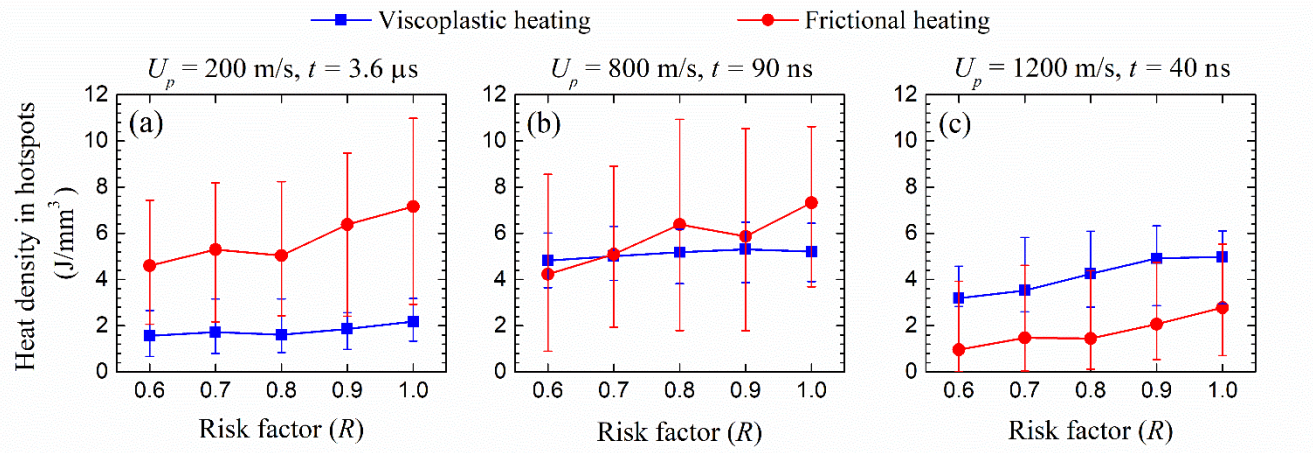

Fig. 11. Comparison of viscoplastic and frictional heating per unit volume in all hotspots with risk factors of $R \geq 0.6$ in PBX9501 samples; (a) $U_p = 200$ m/s, $t = 3.6$ μs, (b) $U_p = 800$ m/s, $t = 90$ ns, and (c) $U_p = 1200$ m/s, $t = 40$ ns.

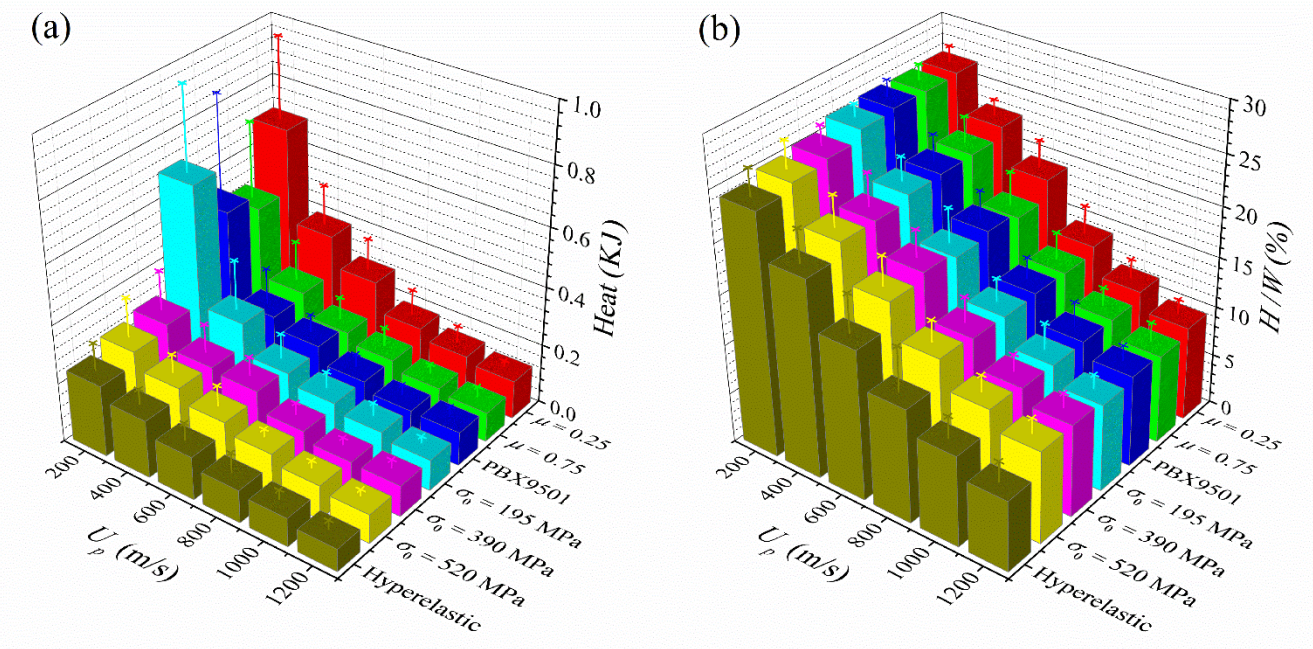

Fig. 12. (a) The amount of heat generated, and (b) the fraction of input work converted to heat, at the time of ignition for all cases over the range of piston velocities of 200-1,200 m/s.

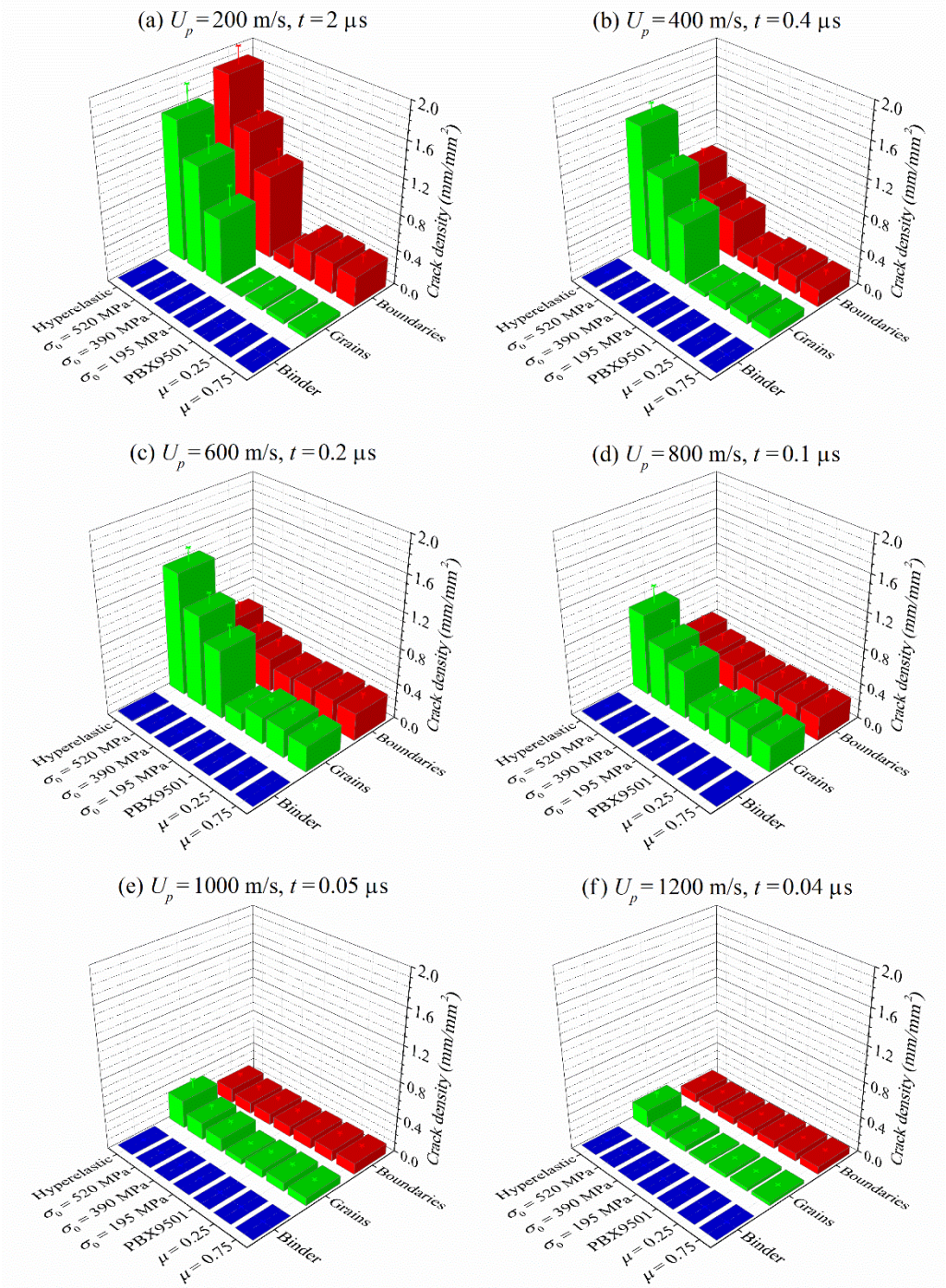

Fig. 13. Densities of cracks at the binder, grains, grain/binder boundaries; (a) $U_p = 200\,\text{m/s}$, $t = 2\,\mu\text{s}$, (b) $U_p = 400\,\text{m/s}$, $t = 0.4\,\mu\text{s}$, (c) $U_p = 600\,\text{m/s}$, $t = 0.2\,\mu\text{s}$, (d) $U_p = 800\,\text{m/s}$, $t = 0.1\,\mu\text{s}$, (e) $U_p = 1000\,\text{m/s}$, $t = 0.05\,\mu\text{s}$, and (f) $U_p = 1200\,\text{m/s}$, $t = 0.04\,\mu\text{s}$.

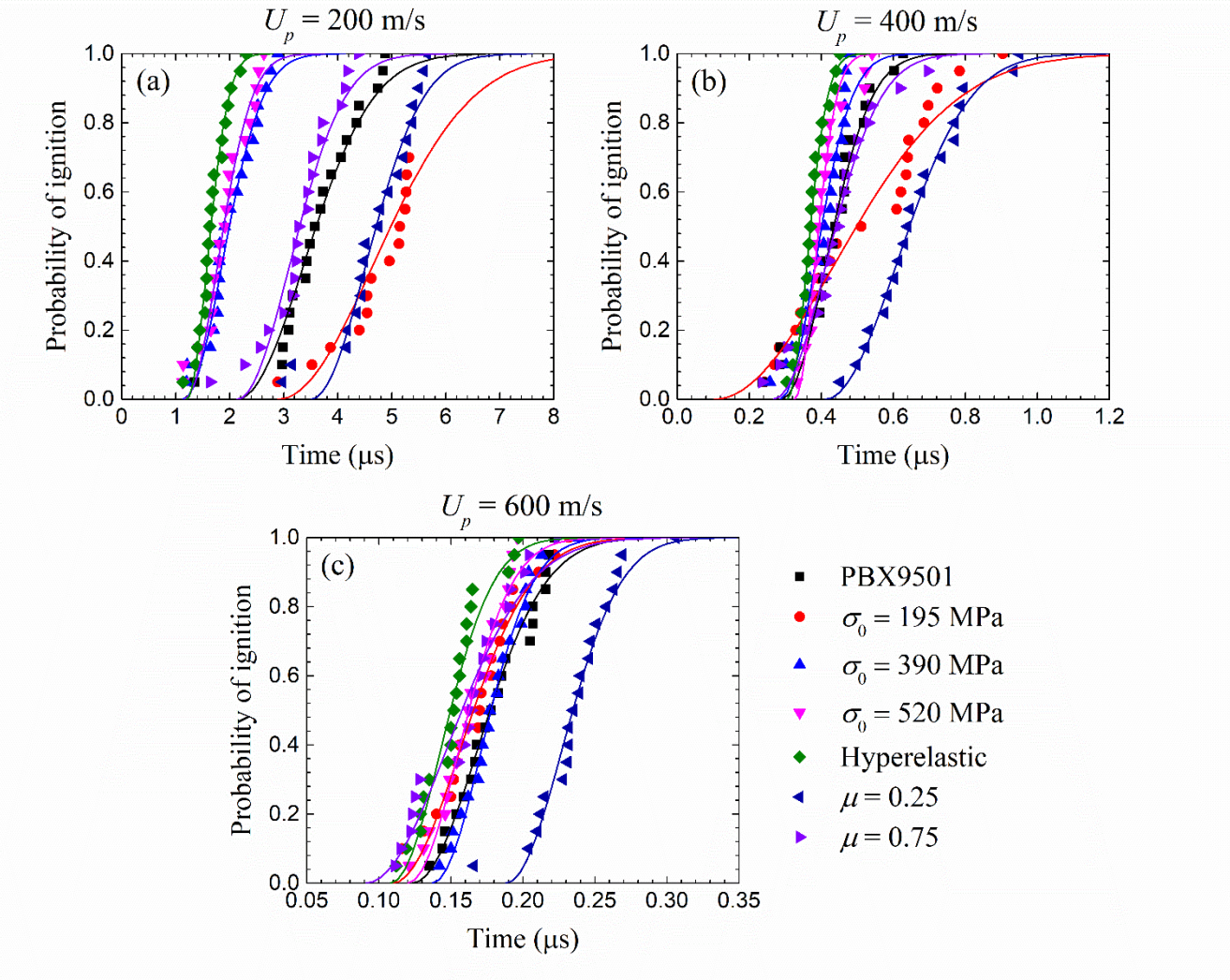

Fig. 14. Distribution of the ignition probability (symbols) and the corresponding Weibull fit (solid lines); (a) piston velocity of 200 m/s, (b) piston velocity of 400 m/s, and (c) piston velocity of 600 m/s.

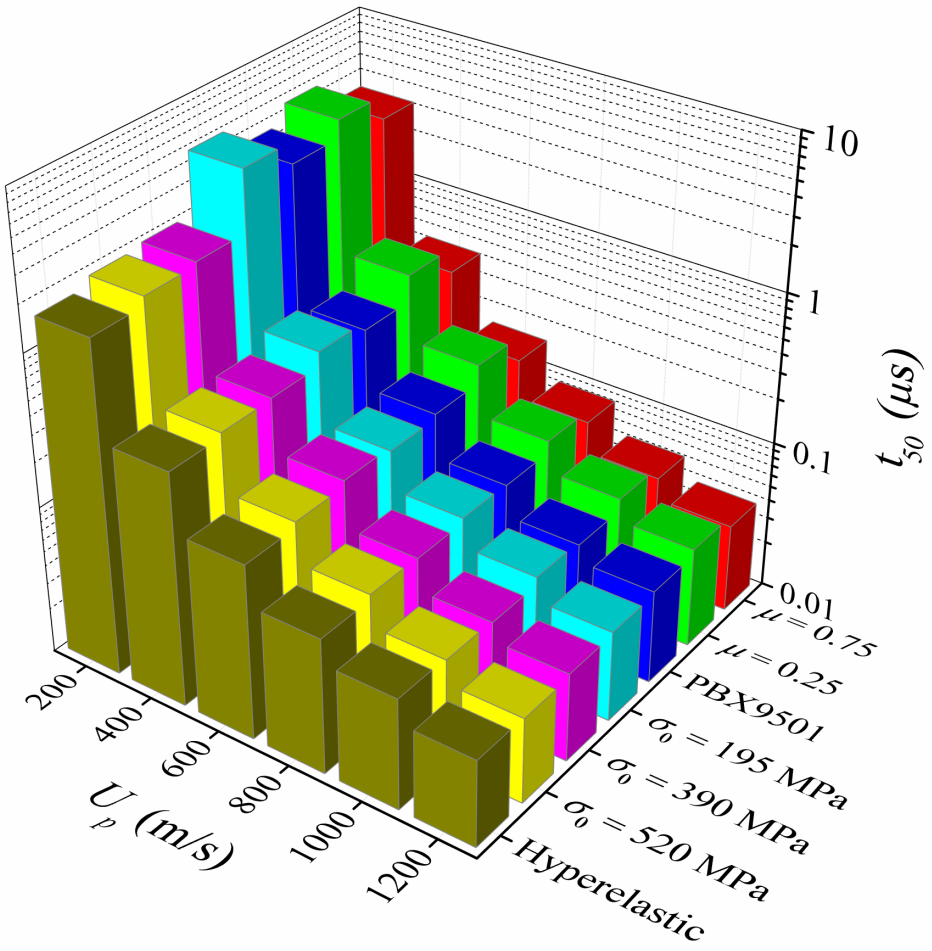

Fig. 15. Median time to ignition as a function of load intensity and levels of constituent plasticity and friction.

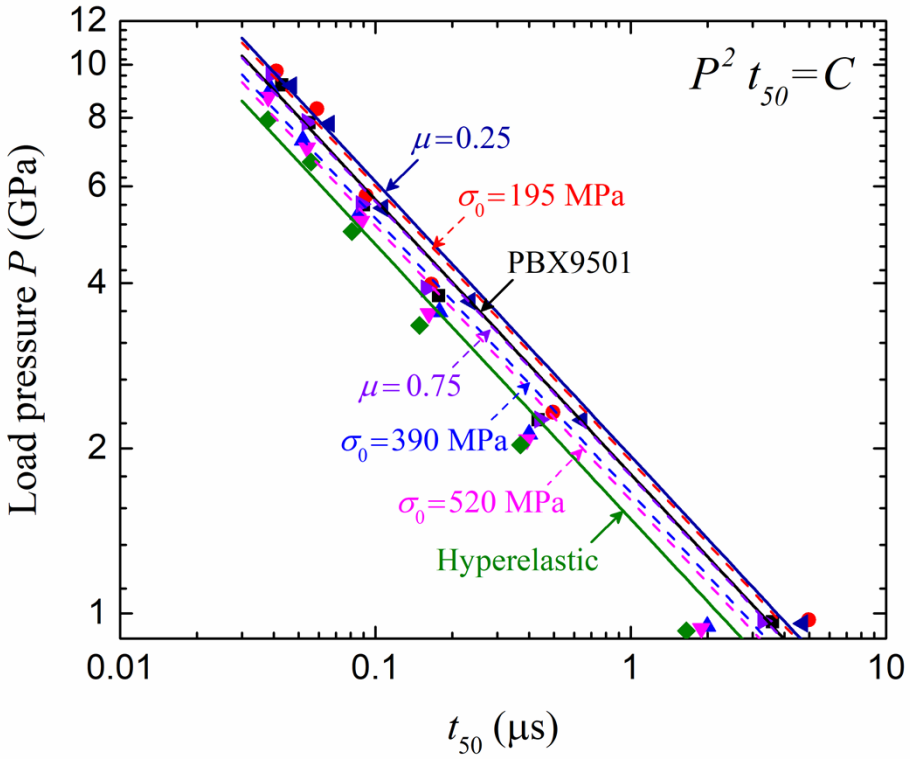

Fig. 16. Comparison of 50% ignition thresholds for PBX9501 and its six variants.